

Compact Itinerant Microwave Photonics with Superconducting High-Kinetic Inductance Microstrips

Samuel Goldstein¹, Guy Pardo¹, Naftali Kirsh¹, Niklas Gaiser², Ciprian Padurariu², Björn Kubala^{2,3}, Joachim Ankerhold², and Nadav Katz¹

¹*The Racah Institute of Physics, The Hebrew University of Jerusalem, Givat Ram, Jerusalem 91904, Israel*

²*Institute for Complex Quantum Systems and IQST, University of Ulm, 89069 Ulm, Germany*

³*Institute of Quantum Technologies, German Aerospace Center (DLR), 89077 Ulm, Germany*

December 28, 2021

Abstract

Microwave photonics is a remarkably powerful system for quantum simulation and technologies, but its integration in superconducting circuits, superior in many aspects, is constrained by the long wavelengths and impedance mismatches in this platform. We introduce a solution to these difficulties via compact networks of high-kinetic inductance microstrip waveguides and coupling wires with strongly reduced phase velocities. We demonstrate broadband capabilities for superconducting microwave photonics in terms of routing, emulation and generalized linear and nonlinear networks.

1 Introduction and motivation

Itinerant optical photonics [1–4] was made possible by the low loss, short wavelength, and controlled patterning in optical on-chip devices, enabling multimode interferometry. Aside from demonstrating superposition and multi-partite entanglement, these systems are proposed as a path to quantum-technological applications [5–7]. A clear and persistent disadvantage of these devices is the challenge of on-demand single optical photon generation [8].

In contrast, superconducting circuits demonstrated high quality, on-demand single microwave photons more than a decade ago [9]. As superconducting qubit systems emerge as a leading candidate in the race towards universal quantum computing, it is vital to integrate microwave photonics for routing, processing and communication between computational nodes [10–12].

The ubiquitous frequencies of microwave quantum circuits are constrained between $\sim 10^9$ - 10^{10} Hz [13,14] due to a combination of fundamental and technical considerations [15]. This leads to typical wavelengths, λ , in excess of 10 mm and enlarged overall device sizes, with consequent box-mode parasitic excitations and fabrication difficulties when trying to scale to complex networks of microwave photonics [16,17]. It has been suggested to compress

footprints by deforming the traces to spirals or meanders [18, 19]. However, such elongated devices are more vulnerable to fabrication errors leading to "weak spots" [20] and increased noise from magnetic vortex penetration [21].

The high-kinetic inductance (HKI) of amorphous superconductors (such as WSi) along with a large microstrip capacitance introduced in this work, allows us to achieve impedance-matched short wavelength microwave photonics. This fulfills the linear networking properties considered above. In addition, the nonlinearity [22, 23] of such HKI microstrips provides a route to amplification at the quantum limit [19, 20, 24–26] due to wave-mixing phenomena. Single HKI superconducting strips have been used to build high-quality microwave resonators [27], superinductors for use in qubit architectures [28], kinetic inductance detectors [23, 29–31], galvanometers [32], and more. This can now be extended to a multi-mode network for more complex photonic tasks.

Here we establish a scalable platform for itinerant microwave networks by demonstrating a variety of geometries of superconducting HKI WSi coupled microstrips. We achieve controllable links between the $50\ \Omega$ impedance-matched central traces by using sub-micronic [33] coupling traces.

This paper is structured as follows: In Section 2 we briefly review the concept of high-kinetic inductance, show how we adopt the microstrip geometry for coupled superconducting networks, and derive the theory of propagation along microstrips connected periodically by coupling traces. For our simplest device this leads to a two-mode bandstructure calculation. This section also describes the simulation of our devices for an arbitrary geometry. Section 3 describes the fabrication of our devices, including design choices made in anticipation of the physical phenomena we want to observe, and the technical recipe for fabrication (extended details are provided in Appendix B). In Section 4 we present the results of experiments with networks of traveling and standing waveguides, and we discuss their linear and nonlinear behavior. Finally, Section 5 considers various applications of our findings. Appendices contain more information on the phase velocity's experimental value, the technical details of the fabrication, the Fabry-Perot resonances in the coupled mode formalism, and specific supporting simulations.

2 Theoretical Framework

2.1 High-Kinetic Inductance Waveguides

The kinetic inductance in superconducting devices operated in the microwave regime stems from the the kinetic energy per unit length associated with the motional energy of the Cooper pairs in the device [34]. The kinetic energy of a single Cooper pair is $\frac{1}{2}(2m_e)v_s^2$, where m_e is the electron mass and v_s is the velocity. The density of pairs equals half the density of electrons n_e , so the kinetic energy per unit length can be written

$$E_k = \frac{1}{2}(2m_e)v_s^2 \cdot \frac{n_e}{2} A = \frac{m_e}{2q_e^2 n_e A} I^2 \quad (1)$$

where A is the cross section. Also $I = q_e n_e v_s A$ is the current, where q_e is the elementary charge. E_k is thus added to the energy of the magnetic field E_m induced when the charge carriers are set in motion [35]. We use the common definition of the total inductance

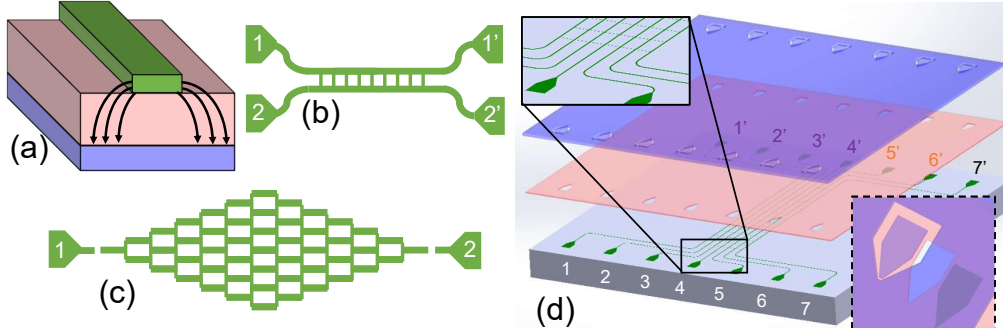


Figure 1: Graphic representation of the microstrip devices. (a) Conceptual microstrip trace geometry; arrows indicate the electric field. Green: superconducting WSi trace, pink: dielectric, purple: Al ground. (b) The double-line device: Two periodically coupled traveling waveguides. (c) The resonant lattice structure, 49 nearest-neighbor coupled standing waveguides, with additional capacitive couplings to launchers in either end. (d) Illustration of the generalization of (b) to seven parallel microstrip traces (the 7PMT), also showing the various layers of fabrication. Note the inversion compared to (a); in our fabrication scheme the WSi is deposited first, and the ground last. Top-left corner inset: Zoom, showing traces and coupling lines. Bottom-right inset: Angled top view, showing the opening in Al and Si layers, fitting the launch pad of the WSi seen as shadow.

per unit length as related to the total energy due to current (also per unit length) by $E_k + E_m = \frac{1}{2}L_l I^2$. Thus the L_l of a superconducting transmission line is comprised of the sum of the kinetic term and the magnetic contribution [36]:

$$L_l = \frac{\mu_0 \lambda_L^2}{A} \left(1 + \left(\frac{I}{I_\star} \right)^2 + \dots \right) + L_{g,l} \quad (2)$$

where μ_0 is the vacuum permeability, λ_L the London penetration depth (~ 450 nm for our WSi traces), and is given by $\lambda_L^2 = m_e / \mu_0 n_e q_e^2$ [37]. In this expression, we have also added I_\star as the characteristic current scale for nonlinearity [24, 38]. The geometric (magnetic) inductance per unit length, $L_{g,l}$ is typically negligible compared to the HKI (first term in L_l) for our thin WSi traces [39].

The nonlinear kinetic inductance (given by the factor $(I/I_\star)^2$ in Eq. (2)) becomes relevant as larger currents are driven through the traces ($\lesssim I_\star$). The underlying physics explaining this nonlinearity stems from a perturbative suppression of the superconducting order parameter as the current is increased [40], and consequently the pair density is suppressed, resulting in a quadratic (nonlinear) increase in λ_L affecting the prefactor of Eq. (2). In our devices, typically $I_\star \simeq 3I_c$, where I_c is the critical current of the traces [41].

We note that the kinetic inductance is a function of transport properties of the superconducting material (especially the large penetration depth λ_L) as well as geometric parameters (such as the small cross-section A).

2.2 Superconducting microstrips

We achieve characteristic impedance-matching in our microstrips with relative ease. The capacitance per unit length $C_l = \varepsilon_r \varepsilon_0 w/d$ can be engineered to fit L_l to reach the impedance $Z = \sqrt{L_l/C_l} = 50$. Here, ε_r and d are the dielectric constant and the thickness of the dielectric layer, and ε_0 the vacuum permittivity. This contrasts the case of coplanar HKI traces, where extended tapers are required to avoid reflections due to discontinuity in Z [42]. The use of impedance-matched microstrips makes the tapers superfluous, reducing the area further. Microstrip traces are essentially parallel plate capacitors, with transverse electromagnetic fields penetrating the dielectric material separating the ground plane from a conducting trace as displayed in Figure 1(a). When connected directly to larger wire-bond launchers (e.g. our "double-line" device, depicted in Figure 1(b)), the microstrips constitute traveling waveguides. Alternatively, standing waveguides, can be implemented with microstrips, when the traces are open or grounded at either end.

Transmission between adjacent microstrips is achieved through sub-micronic coupling wires ("couplers"). As the couplers' widths are narrowed down to about 1/10 of the 50 Ω waveguides' width, L_l of the former is increased by an order of magnitude. Following these geometric changes also C_l changes its value to become smaller by the same ratio. Thus the couplers behave as mostly inductive links. The couplers' Z_l is therefore an order of magnitude larger than that of the waveguides, confirming their perturbative role as a weak link.

A fundamental advantage of the microstrip architecture is the very slow phase velocity (approximately 1% of the vacuum speed of light),

$$v_{ph} = c \left(\varepsilon_r \left(1 + \frac{\lambda_1}{d} \coth \frac{t_1}{\lambda_1} + \frac{\lambda_2}{d} \coth \frac{t_2}{\lambda_2} \right) \right) \simeq \frac{1}{\sqrt{L_l C_l}} \quad (3)$$

where $\lambda_{1,2}$ and $t_{1,2}$ are the superconducting penetration depths and thicknesses of the two superconductors; the trace and the ground [30]. In the devices presented in this paper $v_{ph} \simeq 4 \times 10^6$. The immediate consequence for traveling waves (cf. in the amplifier in [43] and in the first two devices shown here) is that the photons are decelerated to spend several nanoseconds in our device, permitting us to shorten the traces significantly and still maintain sufficient wave-mixing or appreciable routing to other coupled waveguides. In the case of resonant structures, waveguide lengths' L can be reduced according to $L = \lambda/2 \sim v_{ph}/2f$ where f is the desired frequency, cf. the operational bandwidth. For our v_{ph} and f 's this corresponds to $L \sim 200 \mu\text{m}$.

2.3 Theory of periodically coupled traveling waveguides

Aiming towards functionalization, HKI microstrip networks, which form periodic one- or two-dimensional structures, are of obvious interest. Here, we present the (linear) theory of two periodically coupled waveguides of infinite length described and analyzed in the language of crystal physics. This approach is easily extendable to multi-trace networks or two-dimensional devices and can serve as starting point for more advanced descriptions including nonlinearities and quantum effects.

A standard transmission line model (see e.g, Reference [17]) yields wave propagation along the various segments of the structure,

$$V_\alpha^l(x_\alpha) = t_\alpha^l e^{ik_\alpha x_\alpha} + r_\alpha^l e^{-ik_\alpha x_\alpha} \quad \text{where } \alpha = p, s, c; \quad k_\alpha = 2\pi f \sqrt{L_\alpha C_\alpha} \quad (4)$$

$$Z_\alpha I_\alpha^l(x_\alpha) = t_\alpha^l e^{ik_\alpha x_\alpha} - r_\alpha^l e^{-ik_\alpha x_\alpha} \quad \text{and } Z_\alpha = \sqrt{L_\alpha/C_\alpha}. \quad (5)$$

The different segments are distinguished by an index l numbering the unit cells and $\alpha = p, s, c$ for primary, secondary and coupler lines, see Figure 2(a), where for the designed double-line, we can assume $Z_p = Z_s =: Z_0$, $k_p = k_s =: k_0$, while $x_{p/s} \in [0, L]$ and $x_c \in [0, d]$. Dissipation can also easily be included. Kirchhoff circuit equations require voltage matching and current conservation for each node, e. g.,

$$t_p^{l-1} e^{ik_p L} + r_p^{l-1} e^{-ik_p L} = V_p^{l-1}(L) \equiv v_p^l = V_p^l(0) = V_c^l(0) \quad (6a)$$

$$0 = I_p^{l-1}(L) - I_p^l(0) - I_c^l(0), \quad (6b)$$

where the first line can be used to rewrite the current in each segment in terms of two voltage node variables it connects. This immediately yields a tight-binding description

$$0 = h_0 v_p^{l-1} + \epsilon v_p^l + h_0 v_p^{l+1} + h_c v_s^l \quad (7a)$$

$$0 = h_0 v_s^{l-1} + \epsilon v_s^l + h_0 v_s^{l+1} + h_c v_p^l \quad (7b)$$

with real parameters for on-site energy and in- and cross-line hoppings,

$$\epsilon = i \left(\frac{2}{Z_0} \frac{1+z_0^2}{1-z_0^2} + \frac{1}{Z_c} \frac{1+z_c^2}{1-z_c^2} \right) \quad \text{and} \quad h_{0/c} = -i \frac{1}{Z_{0/c}} \frac{2z_{0/c}}{1-z_{0/c}^2}, \quad (8)$$

where $z_0 = e^{ik_0 L}$ and $z_c = e^{ik_c d}$ were introduced.

The eigenmodes of an infinite double-line are straightforwardly found by a Bloch-like ansatz

$$\begin{pmatrix} v_p^l \\ v_s^l \end{pmatrix} = \vec{v}_\nu e^{iK_\nu l} \quad ; \quad K_\nu \in \mathbb{C}, \nu = 1, 2 \quad (9)$$

as eigensolutions of

$$\begin{pmatrix} \epsilon + 2h_0 \cos K_\nu & h_c \\ h_c & \epsilon + 2h_0 \cos K_\nu \end{pmatrix} \vec{v}_\nu = 0 \quad \Rightarrow \quad \cos K_{1/2} = -\frac{\epsilon}{2h_0} \pm \sqrt{\frac{h_c^2}{4h_0^2}}, \quad (10)$$

see Figure 2(b), with eigenvectors that are (anti-)symmetric in primary and secondary voltages for two identical coupled lines.

To solve the actual scattering problem for a finite line we write the ansatz for the general solution

$$\begin{pmatrix} v_p^l \\ v_s^l \end{pmatrix} = \sum_{\nu=1,2} a_\nu \vec{v}_\nu e^{iK_\nu l} + b_\nu \vec{v}_\nu e^{-iK_\nu l} \quad (11)$$

and use Equation (6) to express the left/right-going amplitudes of a unit cell by node voltages

$$t_\alpha^{l-1} = \frac{1}{1 - z_0^2} (v_\alpha^{l-1} - z_0 v_\alpha^l) \quad (12a)$$

$$r_\alpha^{l-1} = \frac{1}{1 - z_0^2} (-z_0^2 v_\alpha^{l-1} + z_0 v_\alpha^l) \quad , \text{ where } \alpha = p/s, \quad (12b)$$

where the input and output of a line with N nodes is

$$t_\alpha^L = t_\alpha^0, \quad r_\alpha^L = r_\alpha^0, \quad t_\alpha^R = z_0 t_\alpha^N, \quad r_\alpha^R = \bar{z}_0 r_\alpha^N. \quad (13)$$

The four variables in the ansatz are then determined by four of the eight equations, Equation. (12), involving the known boundary conditions (e.g., the inputs into all lines), while the remaining four equations yield the unknown output variables.

In that manner, one may, for instance, find for the case of a single input, t_p^L into the primary line (and all other inputs set to zero),

$$t_{p/s}^R = \frac{t^{\text{tot}}(K_2) \pm t^{\text{tot}}(K_1)}{2} t_p^L. \quad (14)$$

with

$$t^{\text{tot}}(K_\nu) = \frac{(1 - z_0^2) \sin K_\nu}{(1/z_0) \sin [K_\nu(N + 1)] - 2 \sin [K_\nu N] + z_0 \sin [K_\nu(N - 1)]}. \quad (15)$$

We will explain the specific form of Eqs.(14),(15) in the discussion of the results below.

2.4 Simulation

Besides the band theory for periodic devices explained above, which can give analytical results for the simplest cases, we apply a number of numerical simulations to model different aspects of the physics of the various investigated devices on varying levels of complexity. Here, we describe a generic method usable for arbitrary linear networks and comment how some nonlinear effects can be accounted for, while other more specific approaches are briefly explained in the appendices.

Defining the network geometry, we consider $q = 1, \dots, Q$ nodes, some of which are connected by edges. Besides its length δ_j , each edge $j = 1, \dots, J_q$ connected to node q is characterized by capacitance and inductance per unit length (determined, e.g., by different widths of main traces and nanowire couplers) yielding an impedance Z_j . The edge voltage then can be written (in line with Equation (6)) as

$$V_q(x) = A_q^j e^{ik_j x} + B_q^j e^{-ik_j x}, \quad (16)$$

where x denotes the distance from the q 'th node along the j 'th edge and k_j is the impedance and frequency dependent wave-number. We solve for A_q^j and B_q^j for all Q nodes' $J = \sum_q J_q$ connected edges, but the number of unknowns can be reduced by mapping the connectivity:

$$A_{q_1}^j = B_{q_2}^j e^{-ik_j \delta_j} \quad (17)$$

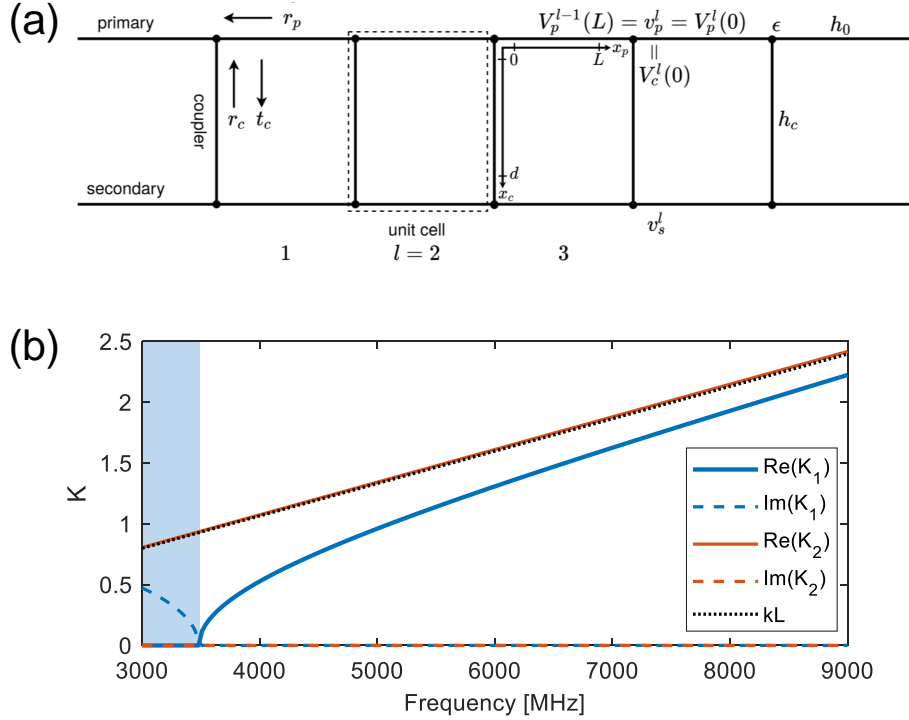


Figure 2: (a) Sketch of the double-trace structure and definitions introduced in the text. Using the voltages on the nodes v_α^l as variables, Kirchoff rules yield a tight-binding model with parameters $\epsilon, h_{0,c}$ as marked on the rightmost unit cell. (b) Bandstructure of a periodic infinite double-line device (parameters adapted from the experimental device). The (Bloch-)wavevector $K_2 \approx kL$ of the eigenmode symmetric in primary and secondary line is nearly unaffected by the couplers, while the anti-symmetric mode has a band gap (shaded region) where $\text{Im} K_1 > 0$.

if the j 'th edge connects the nodes indexed q_1 and q_2 . The input and output nodes (injection and readout) constitute the boundary conditions. For all other nodes current conservation requires that

$$\sum_{j=1}^{J_q} \frac{A_q^j}{Z_j} = \sum_{j=1}^{J_q} \frac{B_q^j}{Z_j}. \quad (18)$$

We encode Eqs. (16)-(18) together with the boundary conditions in a matrix, \mathbf{M} , in which each row represents an equation, so that

$$\mathbf{M} \times \vec{V} = \vec{K} \quad (19)$$

where $\vec{V} = (A_1^1, B_1^1, A_1^2, \dots, A_1^{J_q}, B_1^{J_q}, \dots, A_2^1, B_2^1, \dots, A_Q^1, B_Q^1, \dots, A_Q^{J_Q}, B_Q^{J_Q})$, i.e. the vector of unknowns, and \vec{K} is a vector almost exclusively of zeros due to the nature of the equations, except for those regarding the boundary conditions. Our simulation also accounts for dielectric losses as we add an imaginary term to k_j .

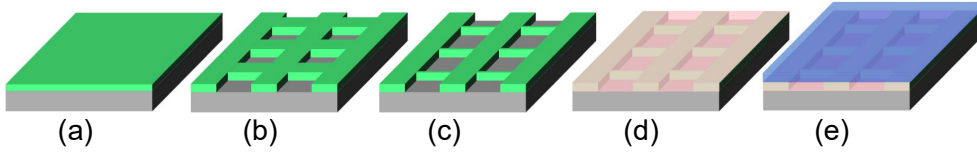


Figure 3: Graphic illustration of the fabrication steps (not in scale). (a) Sputtering of WSi (green) covers the entire surface of the bulk Si substrate (gray). (b) Optical lithography and wet-etch define the network traces. (c) Electronic lithography narrows down the couplers (horizontally oriented in this chart) to the desired submicronic width. (d) aSi (pink) is deposited onto the WSi network, and (e) the Al (ground) is finally added, also by e-beam deposition. The latter layer is subsequently patterned by liftoff (not shown).

Accounting for the nonlinear inductance of our devices leads to a power-dependent wave-equation for each edge, which, in general, yields complicated frequency mixing physics (as exploited for traveling-wave parametric amplifiers [43, 44]). Here, we will not consider those effects, but solve the nonlinear partial differential equation within a single-frequency ansatz (namely with the frequency of the CW-input). Thereby, it reduces to coupled ordinary differential equations (ODEs) for $V(x)$ and $I(x)$ for each segment of our device. In that nonlinear case, we can still encode voltage and current at the nodes (i.e. at the end points of each segment) by amplitudes A_q^J and B_q^j , but the propagation along the segment and the relation between amplitudes at start and end is no longer trivially given by the phase factor of a propagating wave, Equation (17), but rather has to be found by solving the corresponding ODEs for each segment. This means that if nonlinear effects are included for a single segment j between nodes q_1 and q_2 , the two lines in the matrix equation Equation (19) corresponding to Equation (17) (and the corresponding equation linking $B_{q_1}^j$ to $A_{q_2}^j$) are replaced by a nonlinear relation between the four amplitudes, which is implicitly defined by solving the corresponding ODEs. The matrix Equation (19) thus becomes a nonlinear implicit equation.

3 Fabrication

In designing our devices, we consider different aspects directly controlled by the dimensions of the traces. Once the width w and height t of the microstrip are chosen, L_l is settled given its material properties, and the requirement of impedance matching determines the dielectric layer thickness necessary to reach the proper value of C_l .

A central concern of the design is to ensure step coverage. The dielectric layer must necessarily be thicker than the underlying patterned WSi network; when the opposite is the case, the dielectric layer fails to climb and cover the edges of the network, allowing electrical shorts to the ground layer. This constraint disqualifies the use of certain dielectrics, e.g. SiO_2 , with relatively low ϵ_r .

All our devices are fabricated by five consecutive steps to define their three layers. Initially, we grow a ~ 10 nm film of WSi by DC magnetron sputtering, where the stoichiometry of the target (45%/55%) together with the dimensions of the trace, yet to be defined, determines λ_L and hence L_{kin} . A protective resist mask is then applied, first by spinning, and

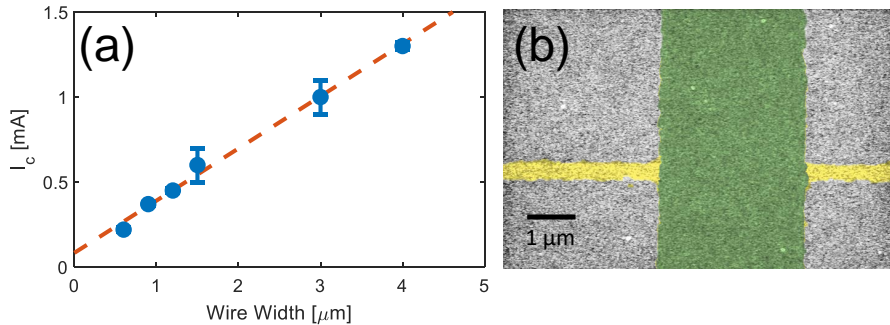


Figure 4: (a) Critical current measurement of a ~ 12 nm thick WSi chip with nanowires of various widths. The dashed line is a linear fit. Reprinted with permission from Reference [46]. © 2021 by the American Physical Society. (b) SEM photo (false-colored) from the 7PMT device of a $3 \mu\text{m}$ wide waveguide (green) and an intersecting submicronic coupler (yellow) connecting the waveguide to parallel waveguides.

next by optical lithography allowing wet-etch of WSi everywhere except on the intended network segments. Electronic lithography is used to narrow the coupler-width from the scale of $\sim \mu\text{m}$, where optical lithography is efficient, to ~ 100 nm, below the wavelength of our laser-writer, again by wet-etch. Next, the dielectric is grown at a rate of ~ 0.1 nm/s by e-beam evaporation without further patterning. The inclusion of dielectrics potentially results in loss effects, considered further below. We choose amorphous silicon with the dielectric constant $\epsilon_r \simeq 11.7$ for this purpose [17].

In the last fabrication step, we prepare a double-layer photo-resist mask. The lower layer’s enhanced sensitivity to the laser compared to the upper layer, results in an ”undercut”, ensuring a smooth liftoff in acetone after evaporation of the Al top film. The Al serves as the electrical ground of the microstrips and protects the device mechanically during continued handling. After dicing into $6 \times 6 \text{ mm}^2$ squares, wire-bonding to impedance-matched printed circuit boards, and mounting in Al boxes, all experiments are conducted at $\simeq 20$ mK temperatures in our dilution refrigerator, far below WSi’s critical temperature of 4.7 K [45].

4 Results and Discussion

Before proceeding to observing the behavior of couplers in networks, we measure their critical currents and find $I_c \simeq 0.15$ mA, which is consistent with the scaling of critical currents with width, found for wider superconducting WSi traces shown in Figure 4(a) [46]. This linear scaling of the critical current with trace cross section emphasizes the advantage of our fabrication method; the e-beam lithography ensures accurate dimensions of couplers and waveguides (exemplified with a SEM photo in Figure 4(b)) and yields the desired nonlinearity.

4.1 Networks of Traveling Waveguides

Our first device, is a "double-line", i.e. two parallel $3\ \mu\text{m}$ wide microstrips, separated by $30\ \mu\text{m}$, and connected every $100\ \mu\text{m}$ by 30 couplers. This periodicity ensures mode coupling under the slowly varying envelope approximation considering the reduced v_{ph} .

We measure the output from both lines (ports 1' and port 2'), when continuous waves (CW) signals are applied from our Keysight P5024A Vector Network Analyzer into one of them (see Figure 1(b)). The total length of each microstrip, i.e. from launcher to launcher, is $3\ \text{mm} > \lambda \simeq 400\ \mu\text{m}$. The unemployed launcher (port 2 in Figure 1(b)) is terminated to the ground through attenuators and a $50\ \Omega$ resistor at room temperature to avoid reflections into the waveguide.

The observed frequency-dependent transmission, Figure 5(a), shows a flat region at low frequencies, where both, direct and coupled, lines transmit well, followed by a series of resonances (anti-resonances) in the direct transmission with concomitant anti-resonances (resonances) in the coupled transmission.

This behavior is well reproduced by simulations of the circuit (dashed) based on voltage continuity and current conservation. To analyze the results, we first consider the eigenmodes of an infinitely extended tight-binding model, see Equation (7). The band structure of the two resulting symmetric and anti-symmetric eigenmodes is shown in Figure 2(b), showing a symmetric mode which propagates with a Bloch-wave vector $K \approx kL$ in the probed frequency range while the antisymmetric mode only emerges above a band gap at $\approx 3.5\ \text{GHz}$. This band structure explains the main features of the observed transmission: Put into line 1 the wave is not in an eigenmode and will excite both modes, which then propagate with different (Bloch-)wave vectors $K_{1,2}$, so that a beating pattern in space results (similar to the physics of evanescently coupled waveguides or coherent oscillations in time in a double-well). The observed resonances and anti-resonances are a direct result of the beating, as is the flat transmission region in the bandgap of the anti-symmetric mode, where the input is split symmetrically into direct and coupled port by the symmetric eigenmode. This simple picture is additionally modified by scattering from the in- and out-coupling into the periodic structure, which leads to small wiggles associated to Fabry-Perot-type resonances, particularly pronounced just above the bandgap (see Appendix C). Other important modifications stem from dissipative effects (although weak), from disorder of the 'crystal'-structure due to fabrication imperfections (see Appendix D) and from any parasitic resonance.

We also observe interference between signals introduced simultaneously in the two waveguides: In Figure 5(b) we alter the phase difference between the two inputs, and while we measure the transmission through one wave-guide, the signal power in the other ("the neighbor") is scanned over four orders of magnitude (and for all relative phases). For the lowest input powers into the neighbor, the direct transmission is drastically reduced due to nonlinearities. This effect is reproduced by our numerical simulation where nonlinearities are present only in the couplers. As the power in the neighbor increases, the signals interfere, and the nonlinearity of the couplers quenches and phase shifts the highest-power signal outputs.

In our next experiment, we increase the network's size to include seven parallel microstrip traces (7PMT) in a circuit similar to the former one, as portrayed in Figure 1(d), which also visualizes the layers of the fabrication scheme. In this device, we boost the couplers'

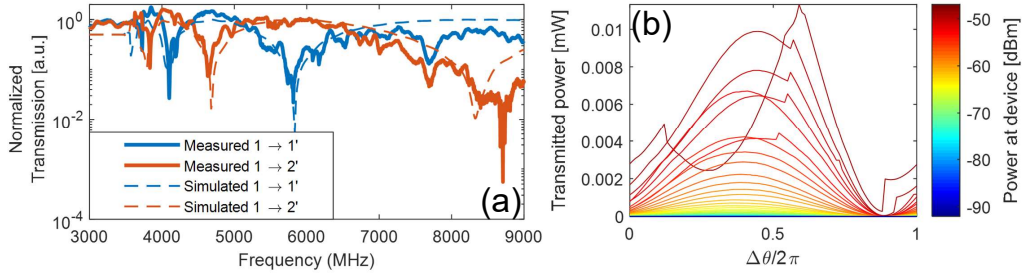


Figure 5: (a) Direct and coupled transmission measurements and simulation for two parallel microstrip traces periodically coupled through highly inductive nano-wires. (b) Phase-dependent transmission, as CW signals are applied in both traces simultaneously, with changing input powers in port 1 (represented by colorbar) and changing phase in port 2 (horizontal axis). The measured output in port 2' (vertical axis).

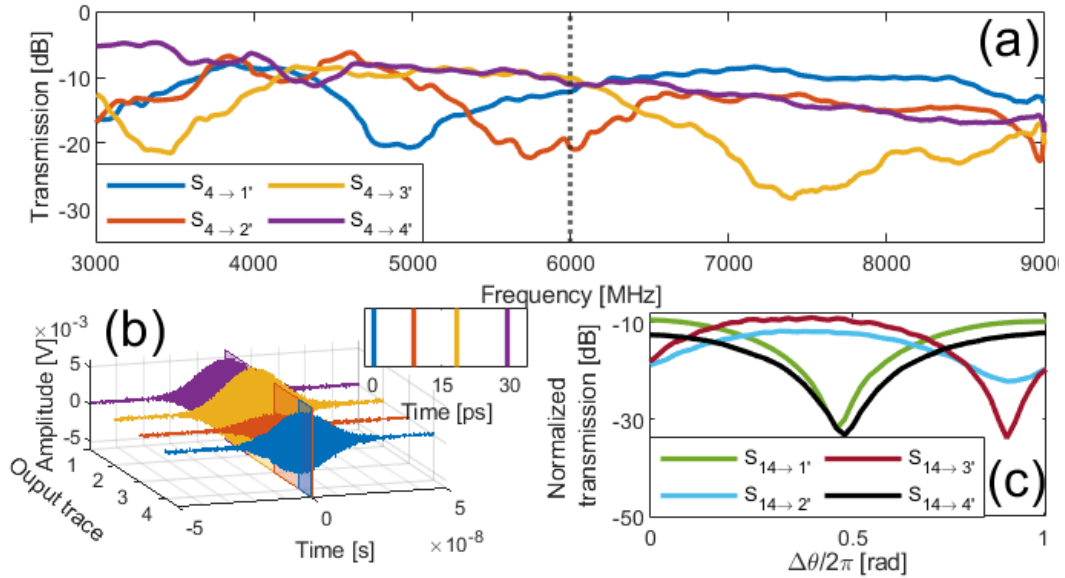


Figure 6: Linear transmission measurements of the 7PMT as described in the main text. (a) Transmission spectra for signals introduced in trace no. 4, with rolling averages of 150 MHz to eliminate ringing caused by minor reflections introduced in connectors. The dotted line at 5.99 GHz marks the central frequency of Gaussian wave packets used in panel (b). (b) Measurement of propagation and arrival times of wave packets with the central frequency f_4 , introduced in the center waveguide. Perpendicular squares mark the center of the wave packet, corrected for unequal launching traces. Inset: Zoom on the (time, output trace)-plane analogue to the colored planes in the main figure. (c) Measured transmission to ports 1'-4', as we split the CW input signal at $f_{1,4} = 5.12$ GHz between port 1 and 4, varying the phase difference.

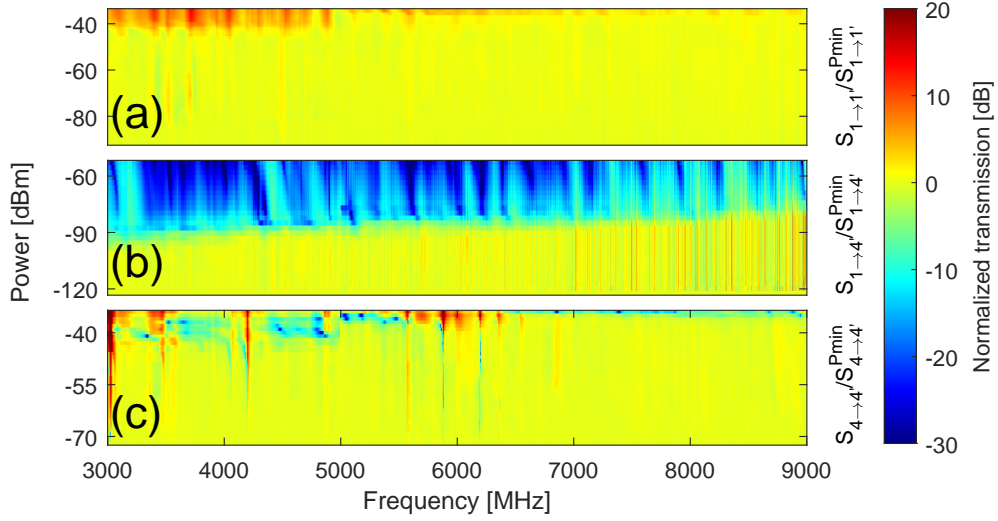


Figure 7: Power transmission spectra in the 7PMT measured for varying input powers, (a) through trace 1, (b) from port 1 to port 4', and (c) through trace 4. Labels are the same as in Figure 1(d). The color-scale is common for all three subfigures, and indicates the power-dependent transmission normalized to the transmission of the lowest power (P_{min}) in the spectrum.

Z_l further by removing the ground above them (not shown), thus minimizing their C_l . The performance is tested by applying CW signals over a bandwidth of 6 GHz in the center trace (no. 4) and measuring the output, presented in Figure 6(a). Here the dotted vertical line marks the frequency $f_4 = 5.99$ GHz, chosen as the central frequency of wave packets used for the subsequent measurement. We then replace the CW signal with short Gaussian-shaped wave packets generated by side-band mixing control, again introduced in the center trace. Their arrival is detected at the output terminals of the device. Overall, each wave packet traverses the network in nanoseconds, but when we subtract the electrical delay, we register the arrival at different output traces with a relative delay of ~ 10 -30 ps (see Figure 6(b)), compared to the arrival of the first wave packet at port 4'. In this figure, the smaller amplitude of the detected wave packet at port 3' (shown in red) is consistent with the lower transmission due to interference through that specific trace.

Returning to CW signals, we proceed at the frequency $f_{1,4} = 5.12$ GHz for which the eight transmission ratios from ports 1 and 4 to ports 1'-4' (according to annotation in Figure 1(d)) are all relatively high and similar in magnitude. Splitting the input power between the former two, we vary the relative phase and measure the output in Figure 6(c). The nearly symmetrical interference patterns are due to similar transmission coefficients in the network (e.g. $4 \rightarrow 1'$ vs. $1 \rightarrow 4'$). Injection at port 4 has the possibility also to coherently diffuse to traces 5'-7', causing the slight asymmetries in Figure 6(c).

Similar theoretical considerations as for the double-line can be employed for the 7PMT. Besides the band structure and symmetry of the eigenmodes, our simulations (see Ap-

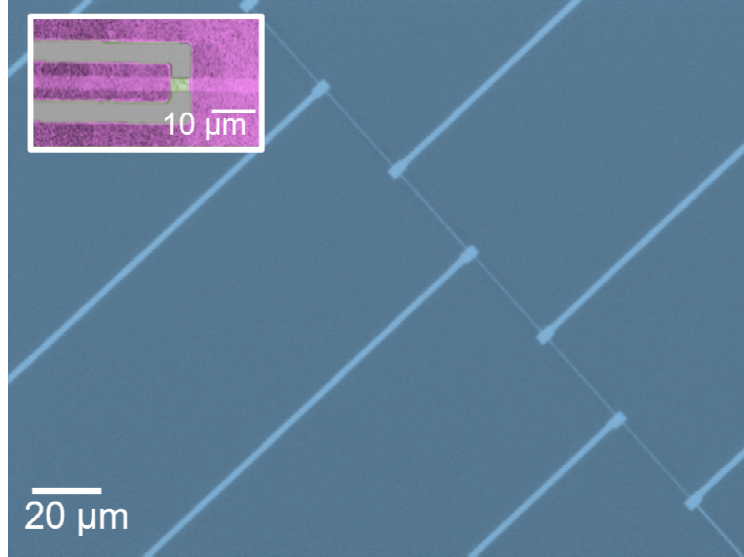


Figure 8: Optical microscopy image (false colored), showing parts of wide microstrip resonators coupled with narrow couplers. Inset: SEM photo of coupling to input or readout with colors matching Figure 6 (grey substrate and green WSi visible in the gap separating purple Al readout line from purple ground).

pendix E) show that propagation through the waveguides resembles quantum walks observed in optical systems [47] with a diffraction pattern, related to the frequency-dependent transmission in Figure 6(a).

We also measure the nonlinearity in the 7PMT emerging from the HKI of WSi by transmitting CW signals of increasing powers through chosen waveguides, starting at signals corresponding to an occupation of ~ 1 photons in the device. The frequency-dependent transmissions, plotted in Figures 7(a)-(c), clearly show that the nonlinearity first emerges in the couplers before it manifests in the waveguides. The direct transmission $S_{1 \rightarrow 1'}$, is thus hardly affected until the highest excitations are reached and the signal is confined in the trace. Transmitting power from this waveguide to the center of the device relies on couplers between all waveguides in between, resulting in the stronger power dependence of $S_{1 \rightarrow 4'}$. The case of transmission through the central waveguide (trace 4) differs from the two above: Despite again considering a coupler-free transmission path, this waveguide is coupled on either side and therefore is more sensitive to the couplers' behaviour. These effects are further discussed in Appendix E (and in its related Figure 13).

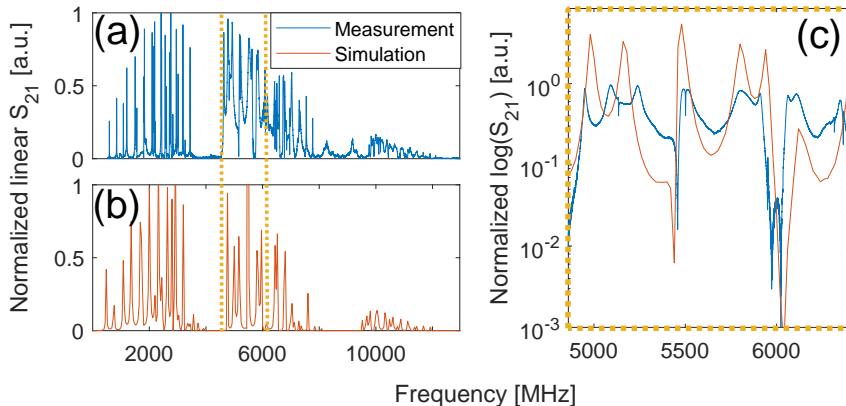


Figure 9: Linear transmission vs. frequency normalized by the the strongest response shown by (a) measurement and (b) simulation. For this device there are only two ports, 1 and 2. Here and elsewhere $S_{x \rightarrow y} = P_y/P_x$, where P_i is the power at port i . (c) Zoom on part of the spectrum joining a and b.

4.2 Resonant Cavity of Standing Waveguides

The third and final demonstration of the capabilities of superconducting microstrip WSi circuitry switches the focus from traveling to standing waves in a 2D square lattice (2DSL) of 49 microstrips, effectively acting as a multi-mode resonance cavity. Each microstrip resonator is $\sim 400 \mu\text{m}$ long and is coupled to four neighbors (two in either end, shown in Figure 8). The resonators in the two opposing corners of the 2DSL are capacitively coupled to coplanar transmission lines (inset of Figure 9(a)), terminated in large (0.3 mm wide) launch-pads, enabling excitation and measurement. Scanning CW the transmission spectrum (Figure 9(a)) reveals three distinctive energy bands within the operational bandwidth of our readout-chain, comparable to the linear simulation in figure 9(b), which considers both dielectric loss and the transmission profile of attenuators, amplifiers, and circulators applied in the experiment. The simulation, analogous to that in Figure 5(a), also correctly reveals finer features within the energy bands (Figure 9(d)), and shows the band structure to be largely determined by the couplers. When these are longer, bands and gaps are dense, as modes populate the couplers. In the opposite limit, reduction of the coupler length breaks down the well-ordered band structure. Importantly, our measurements span several orders of magnitude in power, starting from $P = -120 \text{ dBm}$, which corresponds to an expectation of 0.2 photons within our device (given by $PL/(hf v_{ph})$, with h Planck's constant, $f = 6 \text{ GHz}$, and $L = 3 \text{ mm}$ for the 7PMT traces). Remarkably, the nonlinearity of the couplers confines the transmission in Figure 7(b) at -90 dBm corresponding to only 200 photons.

The 2DSL's geometry is closely related to that of photonic gratings employed to demonstrate a variety of many-body problems [48], such as quantum entanglement [49], interacting polaritons [50], and phase transitions of Mott-Insulators [51, 52].

4.3 Estimating the Kerr nonlinearity

Nonlinearity is observed in the 2DSL, when we introduce sufficiently strong powers and it affects the resonance frequencies' phase and magnitude (exemplified in Figures 10(a) and (b) respectively). The observed behavior can be explained by a Duffing-type toy-model of a Fabry-Perot resonator (see theory results in the insets), where the phase accumulation, when crossing the mirrors and the cavity itself, is assumed to become power dependent (see Appendix G).

The observed power dependence is quantified as a self-Kerr nonlinearity [53], and is approximated as the linear shift in frequency per additional photon, i.e.

$$K_{11} \sim \frac{\Delta\omega}{\Delta N} = \frac{2\pi(f_1 - f_0)}{N_1 - N_0} \quad (20)$$

where $f_{0,1}$ are the resonance frequencies at two different powers, and $N_{0,1}$ the corresponding number of photons in the cavity. The frequency dependence on the photon number is estimated by means of the Q-factor:

$$N = \frac{2P Q}{\hbar\omega \omega} \quad (21)$$

where P is the power. The first fraction in Equation (21) is the rate of photons entering the resonator, and the second fraction is the average survival time of a photon.

For the resonance shown in Figure 10 at powers of -40 dBm and -55 dBm, we find $K_{11} \simeq -7.8 \times 10^{-4}$ Hz. The frequency decreases, when photons are added, so K_{11} is negative, but its magnitude is remarkably larger than the corresponding results found for $w = 8 \mu\text{m}$ [46], consistent with $K_{11} \propto 1/L_{kin}^2 \propto 1/w^2$, cf. Equation (2). Note that the investigated resonance is an extended mode residing in a network of multiple coupled resonators. The mode volume is significantly enhanced and the nonlinearity is therefore somewhat suppressed. When a single resonator is probed, the nonlinearity can be ~ 2 orders of magnitude larger [46].

4.4 Dielectric losses

The use of a thin dielectric barrier for the microstrip capacitance leads to losses from two-level-systems (TLSs) in the dielectric material [54–56]. Powers above a certain material-dependent threshold saturate the TLSs, and the resulting transmission spectrum reflects the nonlinearity of the dielectric rather than that of the waveguide. This effect can be roughly estimated quantitatively by the saturation parameter, a function of the TLS Rabi frequency [57].

However, the short length (up to 10's of wavelengths) of the itinerant devices ensures minimal losses ($< 10\%$), when using a low loss-tangent ($< 5 \times 10^{-4}$) barrier material such as amorphous Si. In future designs an alternative dielectric could replace amorphous Si to allow even higher transmissions and thus signals closer to the single-photon-limit.

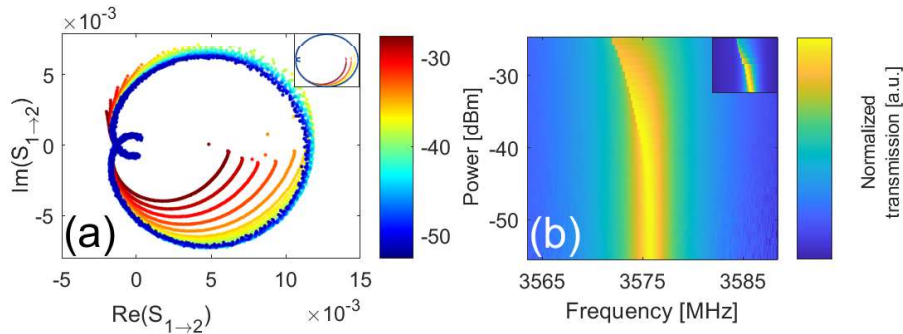


Figure 10: (a) Nonlinearity of the 2DSL measured by a polar representation of the transmission S_{21} in one of the peak frequencies from Figure 9(b) (inset: simulation) and (b) magnitude of the transmission around the same peak frequency as shown in (a) (inset: simulation).

5 Outlook

In this work, we have introduced a platform for on-chip microwave photonic experiments with superconducting circuits. Our three devices, fabricated with established cleanroom procedures, utilize the HKI of WSi in a microstrip geometry. This property, together with the strongly reduced phase velocity, allows us to demonstrate rich phenomena of linear and non-linear optics in on-chip impedance-matched networks of coupled microwave transmission lines.

The three setups presented here constitute first examples of functionalized devices in this platform. They are chosen to demonstrate the possible design versatility that can be advanced to future devices with greater functional complexity. The first setup realizes the simplest linear optics device, a beam splitter [58], by replacing the wave coupling of similar devices in integrated optics [5, 7] by periodic couplers. The crystal like-structure enriches the design variability by the ability to employ band-structure design techniques, for instance, with the aim of creating photonic band gaps or other device principles from photonic crystal or semiconductor physics. In addition, we demonstrated strongly nonlinear effects in the CW propagation. Secondly, we extended the double-line device towards a more complex network, which mimics multi-scatterer configurations used for boson-sampling in quantum optics experiment in the visible regime. There, we studied power diffusion between the traces, pulse propagation, and nonlinear effects.

Waveguide lattices of similar type may also be used for (microwave) photonic simulations, while nonlinearities can be exploited for wave-mixing and non-reciprocity [59]. Finally, in the third setup we realized a network of weakly coupled resonators with multiple pronounced resonances. The Duffing-like nonlinear transmission through one such resonance was investigated in detail.

Going beyond the simplest linear optics devices, the platform presented here will be able to implement both linear and nonlinear functional units, either without (passive) or with (active) external parameter modulation. For instance, passive linear devices could

be built exploiting band structure design to create low or high pass filters, or by designing destructive interference to achieve zero transparency. Our design flexibility in terms of device geometry can be used to build loop resonators, or side-coupled stub resonators, to shape Fano resonances or other desired transmission profiles [60]. Combined with non-linearity, such devices have all the ingredients for nonreciprocal effects and can be used to design diodes. Other possible nonreciprocal units are active devices, e.g. parametrically driven, which can be applied as routers and circulators [59]. In our platform, such devices can be realized by nonlinear frequency mixing with the signal in a control port of a multi-port geometry, or by direct modulation of linear devices parameters.

While the working principle of these integrated optics devices rely on classical wave physics, subject to modifications, our platform may also find use in scattershot boson-sampling [61], multi-mode few-photon interferometry [62], for analogue simulation of effects such as Hawking radiation [63], or as the non-linear medium exploited for reservoir-computing in neural networks [64].

6 Acknowledgements

We acknowledge the support of ISF grants 963.19 and 2323.19 and of the DFG Grant No. AN336/13-1, the IQST, and the Zeiss Foundation.

Appendices

A Estimating the Phase Velocity

An important property of our microstrip networks is the phase velocity, v_{ph} which depends on frequency and geometry of the traces. For the couplers, the geometric inductance, $L_{g,l}$ is completely negligible, and in the linear regime Equation (2) reduces to

$$L_l = \frac{\mu_0 \lambda_L^2}{(t \cdot w)}, \quad (22)$$

where w and t are the width and thickness of the trace in question (written explicitly instead of A). But also $C_l \propto w$, so for traces with submicronic ranges, $v_{ph} = (C_l L_L)^{-1/2}$ is independent of w . However, in wider traces such as our wave guides, $L_{g,l}$ becomes important, hence raising the total L_l somewhat, and lowering v_{ph} by $\sim 10\%$. Wave-guides and couplers are thus foremost differentiated by their impedance Z .

We estimate $\lambda_{WSi} \sim 450$ nm for our sputtered $W_{0.55}Si_{0.45}$ based on other measurements (not shown here), which is in the same order of magnitude, but moderately lower than more tungsten-rich alloys [65].

Our measured $v_{ph} = 4 \times 10^6$ m/s fits its theoretical value found using the formulae and values in this section, and the results also agree with the computed microstrip v_{ph} from [30].

B Technical Aspects of Fabrication

In Section 3 we outlined the fabrication scheme’s various steps associated with the three layers of our device. Here we include additional technical details.

After WSi deposition, the applied photo-resist is AZ1505, spun at 4000 RPM. Exposure with a 405 nm laser is followed by development in AZ developer for a minute, and prior to wet-etch, we hard-bake our devices at 120°C for 2 minutes. The etching is done with a tungsten etchant at 3 nm/s (verified in separate experiments), and stopped by immersion in water.

Narrowing the couplers’ width to below the wavelength of the laser-writer includes, as mentioned, electronic lithography. A protective mask of PMMA is spun at similar parameters as above, baked at 160°C and exposed at 5 A current and 1600 $\mu\text{C}/\text{cm}^2$ in a pattern of two large rectangles distanced by the desired coupler over each intended coupler strip (which after the former step was $> \mu\text{m}$ wide). The **un**exposed strip between these openings in the mask are centered above the strip to be narrowed, and after development in an MIBK solution the process is completed by an additional wet-etch session.

The dielectric Si is grown as we melt and evaporate bulk Si grains by e-beam. The relatively slow evaporation rate (compared to, e.g. the growth rate of Al, mentioned below) as given in the main text, results in the amorphous surface with the desired dielectric constant. Patterning of the Si layer is unnecessary; the WSi and the overlying Al must be in galvanic contact only at the launcher pads, and the large areas of these two layers ensures a sufficiently high capacitance, and in turn a negligible impedance $Z_C \ll (i\omega C)^{-1}$ for the range of frequencies in our measurements.

In developing the fabrication recipe, we tested two methods for patterning of the Al ground: Sputtering followed by wet-etch (Al etchant) and lift-off of an evaporated Al film. The advantage of the former is the high quality and uniformity of a sputtered metal film, but this method included alignment through the highly opaque Al layer, when exposing the spun photoresist, intended to serve as a protective mask during the etching step.

The alternative, lift-off, includes a two-layer mask. Initially, LOR 5B is spun (rates as above) and baked at 200°C for 5 min, and subsequently AZ1505 is applied, spun, and baked, and the entire wafer is exposed with parameters as given above. No post-bake is necessary, and we deposit a ~ 60 nm film by e-beam evaporation at 0.5 nm/s.

C Fabry-Perot Resonances

The symmetry of the double-line device with respect to exchanging primary and secondary line is reflected in the (anti)symmetric eigenmodes. If the lines were fed by a symmetric combinations of incoming waves, these would couple to the symmetric eigenmode and result in symmetric outgoing waves. Following this reasoning, we can decouple the double-line into two independent single-channel problems: after introducing (anti)symmetric combinations

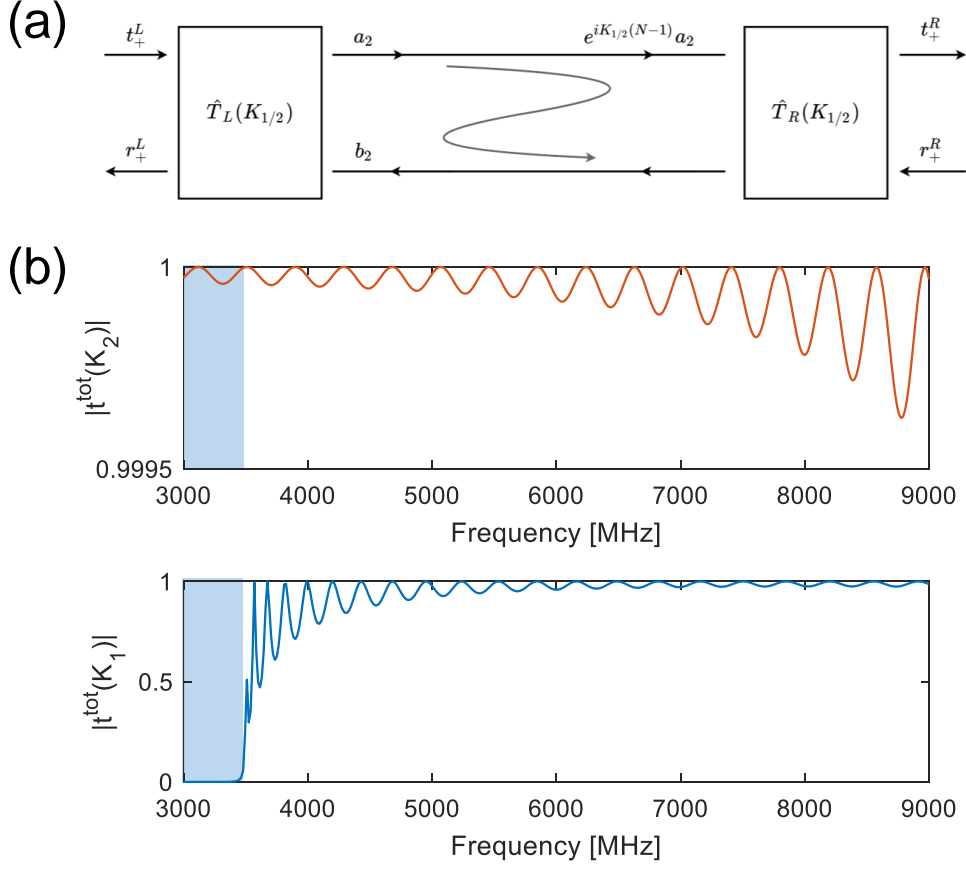


Figure 11: (a) Fabry-Perot resonator formed by scattering at in-/out-coupling and propagation in eigenmode of infinite line. Transmission of symmetric (b) and anti-symmetric eigenmode through the Fabry-Perot structure, cf. Eqs. (15) and (24).

Eqs. 10 and 11 result in

$$t_+^l = \frac{t_p^l + t_s^l}{2} = \frac{1}{1 - z_0^2} \left[a_2 e^{iK_2 l} (1 - z_0 e^{iK_2}) + b_2 e^{-iK_2 l} (1 - z_0 e^{-iK_2}) \right] \quad (23a)$$

$$t_-^l = \frac{t_p^l - t_s^l}{2} = \frac{1}{1 - z_0^2} \left[a_1 e^{iK_1 l} (1 - z_0 e^{iK_1}) + b_1 e^{-iK_1 l} (1 - z_0 e^{-iK_1}) \right] \quad (23b)$$

and equivalent expressions for r_{\pm}^l , so that we indeed arrive at two decoupled single-channel scattering problems.

To understand results, it is instructive to view the single-channel problem as a Fabry-Perot type scattering problem, where in- and out-coupling constitute a left and right scat-

tering barrier of a resonator, in which propagation is described by the eigenmode, see Figure 11(a). Transfer matrices of the individual barriers, $\hat{T}_{L/R}(K_{1/2})$, are then obtained from Equation (23) (and the corresponding equation for r_{\pm}^l) and Equation (15) is recovered from the standard picture of multiple reflections

$$t^{\text{tot}}(K) = \tilde{t}_L e^{iK(N-1)} \left(1 + \tilde{r}_R e^{i2K(N-1)} \tilde{r}'_L + \dots \right) \tilde{t}_R = \frac{\tilde{t}_L e^{iK(N-1)} \tilde{t}_R}{1 - \tilde{r}_R e^{i2K(N-1)} \tilde{r}'_L}, \quad (24)$$

where $\tilde{t}_{L/R}$, $\tilde{r}_{L/R}$, $\tilde{t}'_{L/R}$, $\tilde{r}'_{L/R}$ are entries of the scattering matrices corresponding to $\hat{T}_{L/R}(K_{1/2})$.

This picture allows us to explain the features observed in the total transmissions of the symmetric and antisymmetric single-channel problem shown in Figure 11(b). In the symmetric case, where the eigenmode wavevector $K_2/L \approx k$ (cf. Figure 2(b)), in- and out-coupling occurs with minute reflections, so that the total transmission $t^{\text{tot}}(K_2) \approx 1$ with tiny Fabry-Perot oscillations determined by the $e^{i2K_2(N-1)}$ phase factor in the denominator. In the antisymmetric case, below the bandgap (cf. Figure 2(b)) total transmission is completely suppressed, while above the bandgap large reflection at the in- and out-coupling 'barriers' yield pronounced anti-resonances, which become reduced as K_1 grows to approach kL . The frequency of oscillations is related to the slope of the $\text{Re } K_1(\omega)$ curve in Figure 2(b).

The total transmission involving the excitation and interference of both eigenmodes is easy to understand below and far above the bandgap: In the bandgap of the antisymmetric solution, where $\text{Im}K_1 > 0$, sizeable transmission only occurs through the symmetric eigenmode with $|t^{\text{tot}}(K_2)| \approx 1$ and, hence, $|t_{p/s}^R| \approx 1/2$. Far above the bandgap, both eigenmodes transmit near perfectly in a wide frequency range and alternately interfere constructively and destructively in primary and secondary line, where the frequency of this interchange is determined by the difference in $K_1 - K_2$ stemming from the $e^{i2K_{1/2}(N-1)}$ phase factors in the numerators of Equation (24) resulting in the large-scale structures in the transmission shown in Figure 5(a). Just above the bandgap, substantial interference can only occur, when the antisymmetric transmission peaks due to a Fabry-Perot resonance, but it will also depend on the respective phases. These resonances are closely spaced (cf. Figure 11(b)), and the result is the rather complex transmission pattern between 3.6 and 4 GHz in Figure 5(a). Similar considerations as for the double-line can be employed for multi-line setups, but there, beyond the band structure and some symmetry considerations on the eigenmode structure, an intuitive understanding becomes considerably harder.

D Disorder of the Periodic Structure

For all the simulations presented in this work, we assumed devices to have strictly identical parameters for various segments; i.e., for the double-line device all couplers are assumed to have identical length, impedance and capacitance per length, and are equidistantly placed and primary and secondary line are similarly identical. Fabrication imperfections will obviously disturb these symmetries; both the discrete translational symmetry by one unit cell (periodicity) and the p/s-mirror symmetry. As these symmetries were crucial in explaining the experimental measurements, we study the robustness of observed features against disorder in the parameters of the individual segments. For that purpose, we assume independently, normal distributed parameters for inductance, capacitance and length of each

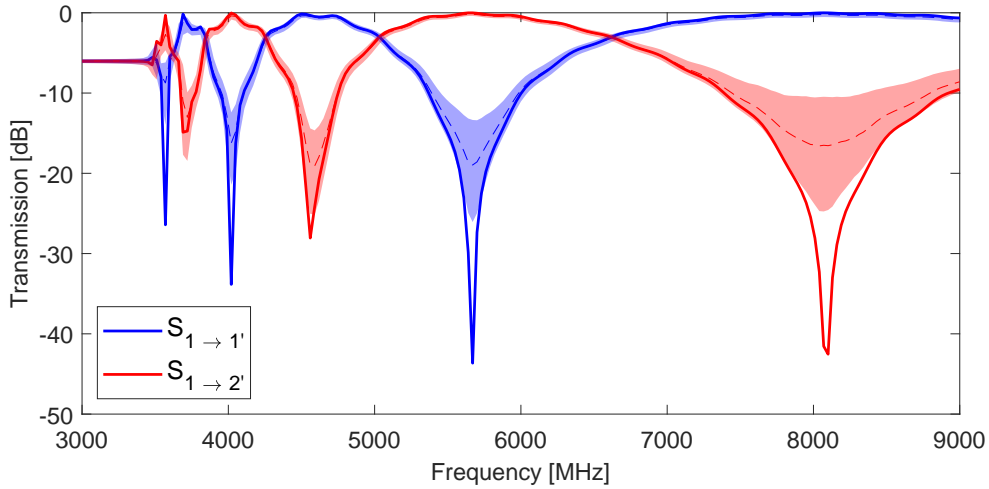


Figure 12: Influence of fabrication imperfection. Direct and coupled transmission through a double-line device without (solid) and with variation of parameters between individual segments.

individual segment with a relative variance 3%. Figure 12 shows the simulation result for direct and coupled transmission (cf. Figure 5(a)) obtained by simulating $N = 1001$ such imperfect devices compared to the device without variations (solid lines). The shaded region indicates a 1σ confidence interval (i.e., for a certain frequency only 16% of devices fall below (above) the lower (upper) limit) around the median (dashed). Note, that the depth of the destructive interference minima is very sensitive to the symmetry breaking caused by disorder, while other features are relatively robust.

E Simulation of Power Propagation in the 7PMT

In the main text we discussed the simulated propagation of power throughout the network, both directly through various traces in the linear regime, and in the nonlinear regime. In Figure 13 we expand the simulation to show the propagation, also in the narrow couplers, too numerous to be shown in the main letter.

In particular, Figure 13(a) displays the delay of transmission from the central trace, where the power is injected, to its neighbors. This is due to the high nonlinearity experienced by most of the couplers linking this trace to the rest. In 13(b), where the introduced power is five orders of magnitude lower, fewer couplers are affected and the power transmits to adjacent traces earlier.

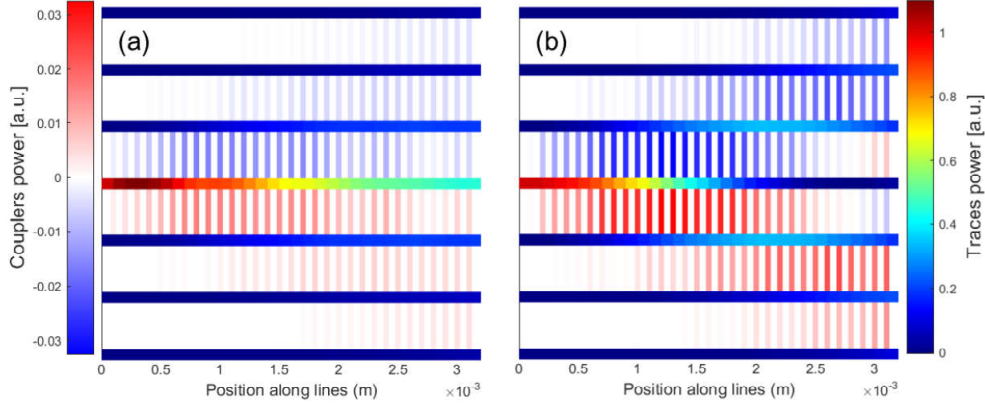


Figure 13: Simulations of power distribution in the 7PMT, when introducing signal at $8.5GHz$ in the central trace at (a) -40 dBm and (b) -90 dBm. Colorbars include direction (positive is defined downwards and rightwards). Left(right) colorbar relates to couplers(traces) in both subfigures. Both figures are normalized according to the input power (i.e. leftmost cell in the central trace equals unity).

F Simulation of the Nonlinear Behavior of the Double-Line

In Section 4 of the main text we discussed the interference between two inputs in the double-line device and showed the impact of nonlinear effects at higher power in Figure 5(b). Here, we will briefly describe, how to use a nonlinear single-frequency simulation to model such effects.

To model the experimental results of Figure 5(b), we consider a nonlinear inductance as in Equation (2) for the couplers only, where nonlinear effects are more pronounced. In Section 4 of the main text we explained how nonlinearities can be included for signal propagation along certain segments and how this modifies the generic matrix equation (19) for a network of arbitrary geometry. The resulting nonlinear problem is solved in Matlab using a Broyden method, within which a standard ODE45-solver is used to find the amplitude relations along each segment. The results of this simulation are shown in Figure 14.

In the experiment we observed at the lowest probed power a transmission with a purely sinusoidal phase dependence. Overall the transmission is drastically reduced as compared to the linear regime of Figure 5(a). For stronger power non-linear effects manifest as modified phase dependence with a pronounced minimum at fixed (power-independent) phase difference, and finally as jumps that signal multi-stable states. While our simulation was not designed to capture multi-stability and possible hysteretic behaviour, it can reproduce some of the observed features such as a modified phase dependence and pronounced minima

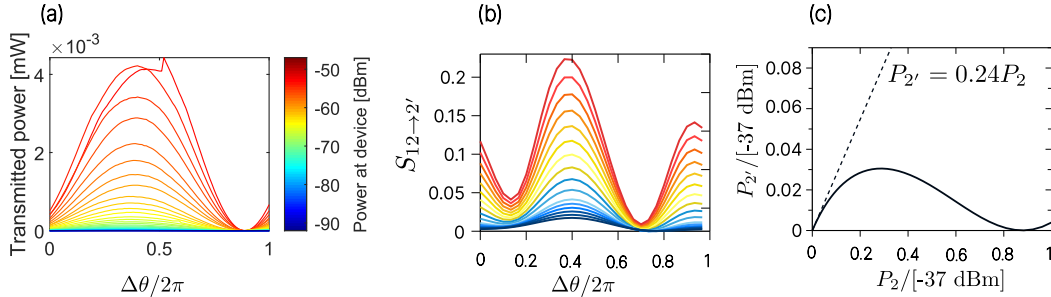


Figure 14: Measurement and simulations illustrating the non-linear behavior of the first device (with two parallel microstrips) in the interference measurement presented in Figure 5(b). Signals are sent down both traces 1 and 2, with constant phase and variable power in trace 1, while in trace 2 the power is kept constant ($P_2 \simeq -37$ dBm) and the phase θ is varied. (a) Measurement curves showing the power output at trace 2' (opposite of trace 2) for different values of the power in trace 1. Non-linear effects manifest as a shift of the phase dependence and jumps that signal multi-stable states. (b) The simulation captures the shift of the phase dependence with increasing power in trace 1. (c) The transmitted power $P_{2'}$ has a linear regime as a function of the input P_2 (with P_1 set to zero) only up to a power $P_2 \simeq -50$ dBm. The measurement $P_2 \simeq -37$ dBm corresponds to the non-linear regime, near the zero of $P_{2'}$, where the transmission is drastically reduced, as can be seen in (a) (the transmission is negligible for $P_1 \simeq 0$).

at fixed phase.

The overall low transmission at the lowest probed power is explained by Figure 14(c). It shows the transmitted power $P_{2'}$ as a function of the input P_2 (with P_1 set to zero) up to the power of $P_2 \simeq -37$ dBm used as the constant reference power in Figure 14 (a,b) and the experiment. The transmitted power $P_{2'}$ has a linear dependence on the input only up to a power $P_2 \simeq -50$ dBm. The measurement $P_2 \simeq -37$ dBm thus corresponds to a strongly non-linear regime, namely an input power near the zero of $P_{2'}$. For Figure 14 (a,b) this means that for the lowest curves (where the power input into P_1 is non-zero but small), the transmission is hence drastically reduced and strongly modulated by the phase of the weak P_1 .

G Simulation of a non-linear resonance in the 2DSL

The resonance studied in Figure 10 is modeled as a resonance of a toy-model Fabry-Perot cavity with Duffing non-linearity, acting as proxy for the much more complex resonant structure realized in the experiment. The output a_{out} amplitude of a Fabry-Perot cavity is related to the input a_{in} at one of the cavity mirrors (port 1) by the total transmission amplitude, $a_{\text{out}} = S_{21}a_{\text{in}}$, which depends on the transmission amplitudes t_1 and t_2 and reflection amplitudes r'_1 and r_2 of the two scatterers (mirrors) defining the cavity:

$$S_{21} = \frac{|t_1||t_2|e^{i\phi}}{1 - |r'_1||r_2|e^{2iK_{\text{eff}}L}}, \quad (25)$$

where we have assumed a symmetric cavity, $|t_1| = |t_2| = t$ and $|r'_1| = |r_2| = \sqrt{1 - t^2}$. Important to the model are the phases $2K_{\text{eff}}L$ and ϕ . The first models the phase accumulated during one round-trip through the cavity, while in the second includes contributions from

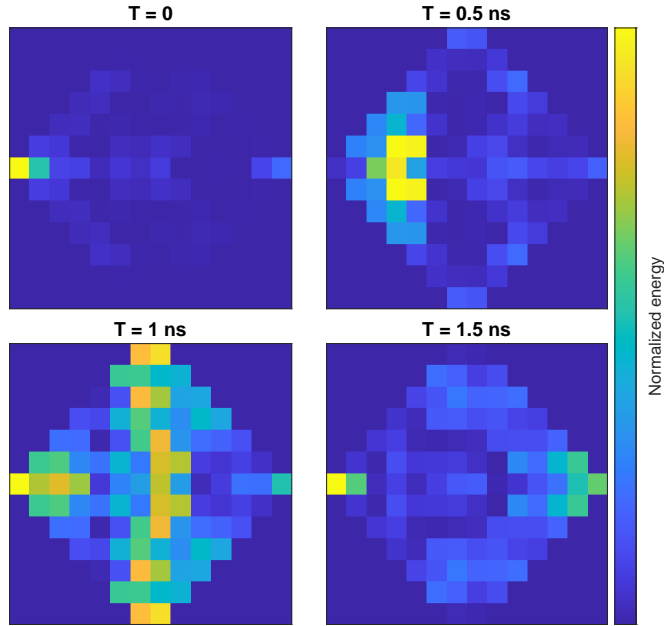


Figure 15: Simulated power propagation of the initial state mainly occupying the left-most resonator. Note that the energy scale in is normalized in each image according to the highest value (which slightly decreases due to loss effects).

passing through the mirrors. Both phases are assumed linear in the input frequency ω in the linear regime and account for a Duffing-type non-linearity by including a power dependence (where $|a_{\text{out}}|^2$ stands in for the intra-cavity intensity),

$$\phi = \frac{(\omega - \omega_{\text{res}})}{\alpha\gamma} \left(1 - \beta \frac{\gamma}{\omega_{\text{res}}} \frac{|a_{\text{out}}|^2}{P_c} \right), \quad (26)$$

$$K_{\text{eff}}L = 2\pi \frac{\omega}{\omega_{\text{res}}} \left(1 + \frac{\gamma}{\omega_{\text{res}}} \frac{|a_{\text{out}}|^2}{P_c} \right). \quad (27)$$

Here we have introduced parameters that characterize the resonance: frequency ω_{res} , linewidth $\gamma = t^2\omega_{\text{res}}$, and critical output power P_c above which the Duffing curve becomes multiple valued. These can be directly extracted from the measurement. The two numerical parameters α and β are the only fitting parameters, that are found to be of order unity. ($\alpha = 2$ and $\beta = 1.6$). With this model, we can reproduce all features of the experimental results for the transmission amplitude S_{21} , as shown by the simulation results in the insets of Figure 10.

H Simulation of the Energy Diffusion

Our simulations elaborate on future experiments possible with a lattice of coupled microwave resonators as the one we produced, though not experimentally possible with the given instantaneous bandwidth of the IQ mixers in our lab. By choosing the 15 highest peaks in the second energy band shown in the main text's Figure 9(b) (between 4.8 and 8 GHz) and their corresponding wave functions $\vec{\psi}_m$ (presumed to be eigenmodes of the system), we simulate the evolution of

$$\vec{\chi}(0) = \sum_m \alpha_m \vec{\psi}_m \quad (28)$$

where $\vec{\chi}(0)$ denotes the state, where only one of the corner-resonators in the lattice is excited. Ideally, if $\vec{\psi}_m$ was a complete set of orthonormal eigenmodes, we would expect $\vec{\psi}_n \cdot \vec{\psi}_m^* = \delta_{n,m}$. This would imply that

$$\alpha_m = \vec{\psi}_m^* \cdot \vec{\chi}(0) \quad (29)$$

In reality, the main text's Figure 9 shows only modes with considerable energy in the two resonators used for input and output respectively. Thus $\vec{\psi}_m$ does not obey Equation (29), but approximates it as the unnormalized wavefunctions holds $|\vec{\psi}_n|^2 \gg \vec{\psi}_n \cdot \vec{\psi}_{m \neq n}^*$. The limitation of this approximation is visible in Figure 15(a), where our attempt to excite only the first resonator also leads to weak excitations in other resonators. The evolution of the states over time and the propagation of the energy throughout the lattice is given by $\vec{\chi}(t) = \sum_m \alpha_m \vec{\psi}_m e^{-2i\pi f_m t}$ and is depicted in Figure 15.

References

- [1] Dmitriev A Y, Shaikhaidarov R, Antonov V, Hönl-DeCrinis T and Astafiev O 2017 *Nature communications* **8** 1–6
- [2] Wang X L, Chen L K, Li W, Huang H L, Liu C, Chen C, Luo Y H, Su Z E, Wu D, Li Z D *et al.* 2016 *Physical review letters* **117** 210502
- [3] Zhong H S, Wang H, Deng Y H, Chen M C, Peng L C, Luo Y H, Qin J, Wu D, Ding X, Hu Y *et al.* 2020 *Science* **370** 1460–1463
- [4] Yang Y, Jin Y, Xiang X, Li W, Liu T, Zhang S, Dong R and Li M 2021 *arXiv preprint arXiv:2101.04078*
- [5] O’Brien J L, Furusawa A and Vučković J 2009 *Nature Photonics* **3** 687–695
- [6] Pirandola S, Bardhan B R, Gehring T, Weedbrook C and Lloyd S 2018 *Nature Photonics* **12** 724–733
- [7] Wang J, Sciarrino F, Laing A and Thompson M G 2020 *Nature Photonics* **14** 273–284
- [8] Chang D E, Vuletić V and Lukin M D 2014 *Nature Photonics* **8** 685–694
- [9] Houck A A, Schuster D, Gambetta J, Schreier J, Johnson B, Chow J, Frunzio L, Majer J, Devoret M, Girvin S *et al.* 2007 *Nature* **449** 328–331
- [10] Huang H L, Wu D, Fan D and Zhu X 2020 *Science China Information Sciences* **63** 1–32
- [11] Flurin E, Roch N, Mallet F, Devoret M H and Huard B 2012 *Physical review letters* **109** 183901
- [12] Juliusson K, Bernon S, Zhou X, Schmitt V, Le Sueur H, Bertet P, Vion D, Mirrahimi M, Rouchon P and Esteve D 2016 *Physical Review A* **94** 063861
- [13] Gao J 2008 *The physics of superconducting microwave resonators* Ph.D. thesis California Institute of Technology
- [14] Malyshev V, Melkov G and Prokopenko O 2020 *Low Temperature Physics* **46** 348–357
- [15] Krantz P, Kjaergaard M, Yan F, Orlando T P, Gustavsson S and Oliver W D 2019 *Applied Physics Reviews* **6** 021318
- [16] Lienhard B, Braumüller J, Woods W, Rosenberg D, Calusine G, Weber S, Vepsäläinen A, O’Brien K, Orlando T P, Gustavsson S *et al.* 2019 Microwave packaging for superconducting qubits 2019 *IEEE MTT-S International Microwave Symposium (IMS)* (IEEE) pp 275–278
- [17] Pozar D M 2011 *Microwave engineering* (John Wiley & sons)
- [18] Morvan A, Féchant M, Aiello G, Gabelli J and Estève J 2021 *arXiv preprint arXiv:2103.09428*

- [19] Bockstiegel C, Gao J, Vissers M, Sandberg M, Chaudhuri S, Sanders A, Vale L, Irwin K and Pappas D 2014 *Journal of Low Temperature Physics* **176** 476–482
- [20] Adamyan A, De Graaf S, Kubatkin S and Danilov A 2016 *Journal of Applied Physics* **119** 083901
- [21] Koch R H, DiVincenzo D P and Clarke J 2007 *Physical review letters* **98** 267003
- [22] Kher A, Day P, Eom B H, Zmuidzinas J and Leduc H 2016 *Journal of Low Temperature Physics* **184** 480–485
- [23] Valenti F, Henriques F, Catelani G, Maleeva N, Grünhaupt L, von Lüpke U, Skacel S T, Winkel P, Bilmes A, Ustinov A V *et al.* 2019 *Physical review applied* **11** 054087
- [24] Eom B H, Day P K, LeDuc H G and Zmuidzinas J 2012 *Nature Physics* **8** 623–627
- [25] Vissers M R, Erickson R P, Ku H S, Vale L, Wu X, Hilton G and Pappas D P 2016 *Applied physics letters* **108** 012601
- [26] Chaudhuri S, Li D, Irwin K, Bockstiegel C, Hubmayr J, Ullom J, Vissers M and Gao J 2017 *Applied Physics Letters* **110** 152601
- [27] Basset J, Watfa D, Aiello G, Féchant M, Morvan A, Estève J, Gabelli J, Aprili M, Weil R, Kasumov A *et al.* 2019 *Applied Physics Letters* **114** 102601
- [28] Gruenhaupt L, Spiecker M, Gusenkova D, Maleeva N, Skacel S, Takmakov I, Valenti F, Winkel P, Rotzinger H, Ustinov A *et al.* 2019 Design and fabrication of a granular aluminum fluxonium qubit *APS March Meeting Abstracts* vol 2019 pp S26–009
- [29] Day P K, LeDuc H G, Mazin B A, Vayonakis A and Zmuidzinas J 2003 *Nature* **425** 817–821
- [30] Mazin B A, Sank D, McHugh S, Lucero E A, Merrill A, Gao J, Pappas D, Moore D and Zmuidzinas J 2010 *Applied Physics Letters* **96** 102504
- [31] Kerman A J, Dauler E A, Keicher W E, Yang J K, Berggren K K, Gol’Tsman G and Voronov B 2006 *Applied physics letters* **88** 111116
- [32] Doerner S, Kuzmin A, Graf K, Charaev I, Wuensch S and Siegel M 2018 *Journal of Physics Communications* **2** 025016
- [33] Niepce D, Burnett J and Bylander J 2019 *Physical Review Applied* **11** 044014
- [34] Meservey R and Tedrow P M 1969 *Journal of Applied Physics* **40** 2028–2034
- [35] Mallory D and Kadin A 1997 *IEEE transactions on applied superconductivity* **7** 2788–2792
- [36] Sypkens S, Faramarzi F, Colangelo M, Sinclair A, Stephenson R, Glasby J, Day P, Berggren K and Mauskopf P 2021 *IEEE Transactions on Applied Superconductivity* **31** 1–4

- [37] Kittel C, McEuen P and McEuen P 1996 *Introduction to solid state physics* vol 8 (Wiley New York)
- [38] Malnou M, Vissers M, Wheeler J, Aumentado J, Hubmayr J, Ullom J and Gao J 2021 *PRX Quantum* **2** 010302
- [39] Marychev P and Vodolazov D Y 2021 *Journal of Physics: Condensed Matter* **33** 385301
- [40] Semenov A D 2021 *Superconductor Science and Technology* **34** 054002
- [41] Semenov A V, Devyatov I A, Westig M P and Klapwijk T M 2020 *Physical Review Applied* **13** 024079
- [42] Klopfenstein R W 1956 *Proceedings of the IRE* **44** 31–35
- [43] Goldstein S, Kirsh N, Svetitsky E, Zamir Y, Hachmo O, de Oliveira C E M and Katz N 2020 *Applied Physics Letters* **116** 152602
- [44] Erickson R P and Pappas D P 2017 *Physical Review B* **95** 104506
- [45] Seleznev V, Divochiy A, Vakhtomin Y B, Morozov P, Zolotov P, Vasil'Ev D, Moiseev K, Malevannaya E and Smirnov K 2016 Superconducting detector of ir single-photons based on thin wsi films *Journal of Physics: Conference Series* vol 737 (IOP Publishing) p 012032
- [46] Kirsh N, Svetitsky E, Goldstein S, Pardo G, Hachmo O and Katz N 2021 *Physical Review Applied* **16** 044017
- [47] Ng K F, Rodrigues M J, Viana-Gomes J, Ling A and Grieve J A 2020 *Optics Letters* **45** 288–291
- [48] Hartmann M J, Brandao F G and Plenio M B 2008 *Laser & Photonics Reviews* **2** 527–556
- [49] Raimond J M, Brune M and Haroche S 2001 *Reviews of Modern Physics* **73** 565
- [50] Hartmann M J, Brandao F G and Plenio M B 2006 *Nature Physics* **2** 849–855
- [51] Jaksch D, Bruder C, Cirac J I, Gardiner C W and Zoller P 1998 *Physical Review Letters* **81** 3108
- [52] Larson J, Damski B, Morigi G and Lewenstein M 2008 *Physical Review Letters* **100** 050401
- [53] Yurke B and Buks E 2006 *Journal of lightwave technology* **24** 5054–5066
- [54] Kirsh N, Svetitsky E, Burin A L, Schechter M and Katz N 2017 *Physical Review Materials* **1** 012601
- [55] Olivier S, Benisty H, Weisbuch C, Smith C J, Krauss T F and Houdré R 2003 *Optics express* **11** 1490–1496

- [56] Tamura H 2006 *Journal of the European Ceramic Society* **26** 1775–1780
- [57] Steck D A 2007 Quantum and atom optics
- [58] Gabelli J, Reydellet L H, Fève G, Berroir J M, Placais B, Roche P and Glattli D C 2004 *Physical review letters* **93** 056801
- [59] Kamal A, Clarke J and Devoret M 2011 *Nature Physics* **7** 311–315
- [60] Limonov M F, Rybin M V, Poddubny A N and Kivshar Y S 2017 *Nature Photonics* **11** 543–554
- [61] Latmiral L, Spagnolo N and Sciarrino F 2016 *New Journal of Physics* **18** 113008
- [62] Goldstein S, Korenblit S, Bendor Y, You H, Geller M R and Katz N 2017 *Physical Review B* **95** 020502
- [63] Nation P, Blencowe M, Rimberg A and Buks E 2009 *Physical review letters* **103** 087004
- [64] Angelatos G, Khan S and Türeci H E 2020 *arXiv preprint arXiv:2011.09652*
- [65] Zhang X, Engel A, Wang Q, Schilling A, Semenov A, Sidorova M, Hübers H W, Charaev I, Ilin K and Siegel M 2016 *Physical Review B* **94** 174509